Diamond & Related Materials 159 (2025) 112762

Contents lists available at ScienceDirect

Diamond & Related Materials

journal homepage: www.elsevier.com/locate/diamond

Comprehensive characterization of DLC films: Comparative insights from NEXAFS and SXES

Thitikorn Chamchuang [a,*], Tsuneo Suzuki [b], Sarayut Tunmee [c], Praphaphon Silawong [d], Peng Guo [e], Aiying Wang [e], Kazuhiro Kanda [f], Keiji Komatsu [a], Hidetoshi Saitoh [a,*]

[a] Graduate School of Engineering, Nagaoka University of Technology, 1603-1 Kamitomioka-machi, Nagaoka, Niigata 940-2188, Japan
[b] Extreme Energy-Density Research Institute, Nagaoka University of Technology, 1603-1 Kamitomioka-machi, Nagaoka, Niigata 940-2188, Japan
[c] Synchrotron Light Research Institute (Public Organization), 111 University Avenue, Muang District, Nakhon Ratchasima 30000, Thailand
[d] Department of Metallurgical Engineering, Faculty of Engineering, Rajamangala University of Technology Isan, Khon Kaen Campus, Khon Kaen 40000, Thailand
[e] State Key Laboratory of Advanced Marine Materials, Ningbo Institute of Materials Technology and Engineering, Chinese Academy of Sciences, Ningbo 315201, China
[f] Laboratory of Advanced Science and Technology for Industry, University of Hyogo, 3-1-2, Koto, Kamaigori-cho, Ako-gun, Hyogo 678-1205, Japan

ARTICLE INFO

Keywords:
Diamond-like carbon (DLC)
Near-edge X-ray absorption fine structure (NEXAFS)
Soft X-ray emission spectroscopy (SXES)
Chemical bonding structure
sp^3/sp^2 ratio

ABSTRACT

Our study focuses on the comparative insights gained from near-edge X-ray absorption fine structure (NEXAFS) and soft X-ray emission spectroscopy (SXES) techniques in the comprehensive characterization of diamond-like carbon (DLC) films. Understanding the quantitative determination of carbon hybridization is essential for unraveling the relationships between structure and properties in carbon-based materials, including DLC films. Although several technologies exist for characterizing the sp^3 and sp^2 carbon content in these materials, our study reveals that direct comparisons of analytical results are limited, highlighting the need for further research and development in this area. This study compares NEXAFS spectra with SXES data for a range of amorphous carbon coatings, including both hydrogen-free and hydrogenated DLC films with varying hydrogen content levels. Our findings highlight the crucial role of hydrogen in modifying the local electronic structure and the sp^3/sp^2 ratios, which have a significant impact on the properties of the films. Films with low hydrogen content demonstrated strong agreement between NEXAFS and SXES results, while hydrogen-rich films exhibited discrepancies due to the influence of hydrogen on the electronic structure. These results highlight the importance of precise characterization and deposition control in the creation of DLC films for advanced applications.

1. Introduction

Diamond-like carbon (DLC) films are amorphous carbon materials characterized by varying ratios of sp^3 (diamond-like) and sp^2 (graphite-like) hybridization, which determines their diverse physical, chemical, and mechanical properties [1,2]. The proportion of sp^3 and sp^2 bonds governs critical attributes such as hardness, wear resistance, low friction coefficient, thermal and electronic conductivity, optical performance, chemical inertness, gas barrier capabilities, and biocompatibility [2–9]. DLC films, with their diverse physical, chemical, and mechanical properties, also exhibit remarkable versatility due to their ability to make these properties through deposition techniques and process parameters. This adaptability has led to widespread applications, including protective coatings for mechanical and automotive parts, cutting and machining tools, electrical and optical devices, gas barrier films, biomedical materials, anti-corrosion coatings, and insulating films [1,2,10]. Additionally, their environmental stability and compatibility with various substrates further enhance their appeal in modern applications [11]. The potential of DLC films in various industries is a promising aspect of our research that inspires optimism and hope for the future of materials science and engineering.

Accurate measurement of the sp^3/sp^2 ratio is essential for understanding the properties and applications of DLC films. DLC films exhibit a wide range of sp^3/sp^2 ratios, ranging from 10 % to 90 % [1,2]. Films with a high sp^3 content are characterized by their tetrahedral carbon structure, which reveals mechanical hardness and high density. Conversely, films with a high sp^2 content, associated with a trigonal carbon structure, are mechanically softer and exhibit lower density [4,11]. In addition to amorphous carbon, DLC films can include a hydrogenated alloy component, with hydrogen (H) content ranging from

* Corresponding authors.
E-mail addresses: s227008@stn.nagaokaut.ac.jp (T. Chamchuang), hts@vos.nagaokaut.ac.jp (H. Saitoh).

https://doi.org/10.1016/j.diamond.2025.112762
Received 3 July 2025; Received in revised form 4 August 2025; Accepted 19 August 2025
Available online 26 August 2025

0 to 50 %, as illustrated in the ternary phase diagram for bonding in amorphous carbon-hydrogen alloys [1,2,12,13]. C−H bonds in these films terminate dangling bonds, stabilizing the sp^3-hybridized carbon network and enhancing both mechanical and chemical properties [14].

The sp^3/sp^2 ratio also strongly affects the electrical and optical characteristics of DLC films. High sp^3 content films typically exhibit increased electrical resistivity and wider optical band gaps, making them suitable for insulation and transparency applications. In contrast, films with a high sp^2 content demonstrate enhanced electrical conductivity and narrower band gaps, aligning with requirements for conductive and absorptive materials [15,16]. Additionally, the chemical inertness of DLC films is strongly influenced by their sp^3/sp^2 bonding ratio. Films with higher sp^3 content exhibit superior resistance to chemical attack and oxidative degradation, owing to their strong diamond-like network [1,17]. By comparison, films with a higher sp^2 content, characterized by graphite-like structures, are more reactive and weaker to oxidative and acidic conditions [18].

DLC films also excel in gas barrier properties due to their dense, amorphous structure and high sp^3 hybridization ratio. This structure minimizes free volume and gas diffusion pathways, making DLC films effective in protecting the substrate from permeation by oxygen, moisture, and other reactive gases [19,20]. Hydrogenation further enhances their barrier performance by reducing voids and dangling bonds that could serve as channels for gas diffusion. These properties make DLC coatings invaluable for improving the durability and performance of materials in electronics, packaging, and other industries [9,21].

Finally, DLC films are widely recognized for their biocompatibility, attributed to their chemical inertness, smooth surface morphology, and resistance to protein adsorption and bacterial adhesion. These attributes make them ideal for biomedical applications, including coatings for implants and medical devices, where they enhance wear resistance, minimize inflammation, and promote favorable cell interactions [22–26].

X-ray spectroscopy, encompassing both X-ray emission and absorption techniques, is crucial for determining the sp^3/sp^2 hybridization ratio within DLC films. By providing detailed insights into electronic configurations, these techniques offer a critical understanding of the bonding states that influence DLC properties [27,28]. Near-edge X-ray absorption fine structure (NEXAFS) spectroscopy, focusing on the C 1*s* absorption edge within the photon energy range of approximately 280 to 330 eV, effectively probes the unoccupied electronic states [29]. The NEXAFS spectra are divided into a pre-edge region, dominated by transitions from the C 1*s* → unoccupied π* orbitals linked to sp^2 sites, and a main edge region, characterized by overlapping C 1*s* → σ* transitions from sp^1, sp^2, and sp^3 bonding states [30–34].

Complementing this, soft X-ray emission spectroscopy (SXES) investigates the occupied electronic states, offering localized structure information [35,36]. The C—*K* emission spectra are segmented into energy regions that correspond to different bonding features: $E < 277$ eV, reflecting the *s*-state and C−H bonds; $277 \leq E \leq 280$ eV, representing sp^2-σ and sp^3-σ contributions; and $E > 280$ eV, indicative of sp^2-π features within the sp^2-σ band [28,35–38]. This segmentation enables an understanding of bonding characteristics in hydrogenated and hydrogen-free DLC films.

Compared to traditional methods, such as Raman spectroscopy or electron energy loss spectroscopy (EELS), X-ray techniques provide a unique combination of sensitivity to specific bonding configurations and spatial resolution. Moreover, their capability to probe both occupied and unoccupied electronic states allows for a more comprehensive evaluation of the DLC structure. This facilitates advancements in materials design for diverse applications, ranging from protective coating to electronic and optical components [1,20,39]. In addition to Raman and EELS, X-ray photoelectron spectroscopy (XPS) and Auger electron spectroscopy (AES) have long served as standard techniques for determining the sp^3/sp^2 ratio in carbon-containing materials. These surface-sensitive methods have been extensively applied for over 5 decades, offering valuable insights into the chemical and bonding states at the surface [40]. Recent comparative studies highlight the strengths and limitations of XPS, AES, Raman, and XANES (including NEXAFS) for characterizing DLC films. While XPS and AES remain essential for surface analysis, NEXAFS and SXES techniques employed in this study provide complementary depth-resolved information. They are more sensitive to local electronic structure, which is particularly advantageous in evaluating amorphous carbon films [41].

NEXAFS, which probes transitions from core electrons (e.g., C 1*s* → π*/σ*), typically samples depths of 5–10 nm and is highly sensitive to surface contamination, including aliphatic hydrocarbons or oxidation layers [42]. In contrast, SXES, which analyzes photon emissions from occupied states, can detect signals from deeper within the sample (~50–100 nm), thereby reducing the impact of surface-bound species and providing a more representative view of the film's bulk bonding environment [28,38,41]. This difference in probing depth explains the observed discrepancies in sp^3 content between NEXAFS and SXES, particularly in hydrogen-rich films, as discussed in Section 3.2 and illustrated in Fig. 9. By combining these complementary methods, this study establishes a stronger framework for understanding the evolution of bonding in DLC films across varying hydrogenation levels.

This study makes a significant contribution to the field by directly comparing NEXAFS and SXES spectroscopic measurements. Our findings not only provide valuable guidance for accurately interpreting quantitative estimates of the sp^3/sp^2 ratio from NEXAFS and SXES analyses, but also significantly advance the understanding and application of DLC film characterization.

2. Experimental

2.1. Materials

Various types of diamond-like carbon (DLC) films were deposited onto single-crystal silicon (Si) wafers with a (100) orientation using established deposition techniques developed through collaborative efforts involving academic, industrial, and public sector institutions. The classification of DLC films follows established categories: ta-C, a-C, ta-C:H, and a-C:H, as referenced in [43–45]. The Si substrates were prepared using chemical vapor deposition (CVD) and physical vapor deposition (PVD), along with variations in deposition parameters.

Before DLC film deposition, the Si wafers underwent a comprehensive cleaning process to remove surface contamination. First, the wafers were sequentially sonicated in distilled water, ethanol, and acetone for 15 min each. This ultrasonic cleaning eliminates mechanical impurities. The substrates were transferred to a synthesis chamber where they were subjected to argon (Ar) ion bombardment for 30 min. This plasma treatment effectively removed native oxide layers and surface-adsorbed hydrocarbons, ensuring a cleaner substrate for subsequent film growth [46]. Subsequently, DLC films were synthesized on the cleaned Si wafers using different techniques. Hydrogen-free DLC films (ta-C/a-C) were deposited using the PVD technique, yielding low H content (≤5 at.%) as confirmed by elastic recoil detection analysis (ERDA). The film density, measured by X-ray reflectivity (XRR), ranged from 2.69 to 2.89 g/cm^3. These include samples labeled N1–1, N1–2, N1–3, K1, and W1.

Hydrogenated DLC films, ta-C:H/a-C:H, were produced using various CVD methods, resulting in films with medium to high hydrogen content and a wide range of densities. The T1 and T2 series exhibit moderate H incorporation, while the T3 series includes films with higher hydrogen concentrations. These differences reflect the influence of deposition parameters on both hydrogen uptake and film compactness. Similarly, the K2 to K10 series exhibits a broad range of H content and density, consistent with the characteristics of hydrogenated DLC.

In contrast, the C1 series films were deposited using a carbon sputtering system (JEOL, VC-100) onto Si wafers to enhance electrical conductivity for microscopy. These films contain moderate H levels and maintain relatively high density, although no Ar ion pre-cleaning was

applied during their preparation. Corresponding film density values are summarized in Fig. 4.

The methods used to determine the H content and film density are described in the following section. Table 1 summarizes the H content, film density, sp^3/sp^2 ratio, and classification of these amorphous carbon films based on SXES and NEXAFS analyses.

A highly oriented pyrolytic graphite (HOPG) reference was used to analyze NEXAFS spectroscopic measurements due to its well-characterized sp^3/sp^2 bonding structure, which ensured accurate normalization of the NEXAFS technique [5,34,47]. In the case of SXES, the sp^3/sp^2 bonding structure is characterized without the use of standard reference materials. This method has been previously reported and validated in the literature [9,48].

Note: Portions of the data for samples N1–3, T1–1, T2–2, and T3–7, specifically film density, H and Ar content, and sp^3 ratio (SXES and NEXAFS), have been previously reported in [48]. These data are revisited here in the context of a broader comparative analysis involving additional techniques and sample sets.

2.2. Film characterizations

The composition of the DLC films, specifically their H content, was analyzed using Rutherford backscattering spectrometry (RBS) and elastic recoiled detection analysis (ERDA) techniques. These techniques were conducted with an electrostatic accelerator (HVEE, 1.7 MV Tandetron Accelerator System 4117 MC+) at the Extreme Energy-Density Research Institute, Nagaoka University of Technology.

The RBS measurements involved irradiating the sample with a 2.0 MeV He^+ beam directed perpendicularly to the surface. The scattered He^+ particles were detected by a solid-state detector (SSD) positioned at an angle of 80° relative to the surface normal. For the ERDA measurements, the same electrostatic accelerator irradiated the sample with a 2.7 MeV He^+ beam. During this process, a separate SSD detected H ions that were ejected from the sample. The resulting ERDA spectra were analyzed using the SIMNRA software, a simulation tool for ion beam analysis developed by M. Mayer. H content was calculated using the atomic fraction method, which determines the ratio of H to the total number of atoms detected. This approach accounts for elemental areal densities derived from SIMNRA-fitted ERDA spectra and is cross-referenced with RBS results for improved accuracy [49].

The densities of the DLC films were determined using XRR on a Rigaku Smart Lab 9 kW horizontal X-ray diffractometer. X-rays were applied to the sample at grazing incidence, with total reflection occurring at the critical angle. A copper target (Cu K_α) operating at 45 kV and 200 mA provided X-rays with a wavelength of 1.541 Å. The incident optic included a Ge (220) × 2 monochromator to produce a parallel beam with a divergence angle of 0.02°. The total reflection was recorded over a scan range of 0–6° with a step size of 0.004°. The film density was determined by fitting the experimental and simulated reflectivity curves using the GlobalFit software [50].

Note: Professor Kazuhiro Kanda provided the film density and H content for the K series at the Laboratory of Advanced Science and Technology for Industry, University of Hyogo, Japan.

2.3. Characterization techniques of electronic configurations

NEXAFS measurements were conducted at the BL3.2U beamline of the Synchrotron Light Research Institute (SLRI), a public organization in Nakhon Ratchasima, Thailand. The synchrotron radiation source used in this study operated at a beam energy of 1.2 GeV from a storage ring, allowing for the investigation of the density of conduction band states in DLC films.

During the measurements, synchrotron radiation was scattered at a 17° angle relative to the sample surface, with the light polarization aligned parallel to the surface at various incident angles. The C *K*-edge spectra were recorded using the partial electron yield (PEY) detection mode. A gold mesh placed in the front of the sample monitored the intensity of the incident photon beam (I_0), facilitating normalization of the PEY signal. The total energy resolution of the system was 0.1 eV, with an estimated wavelength calibration uncertainty of ±0.2 eV [34]. The C *K*-edge spectra were analyzed across the 280–330 eV energy range.

Note: Researchers conducted the NEXAFS analysis of the K series

Table 1
Summarizes the element content, film density, sp^3/sp^2 ratio, and classification of these amorphous carbon films based on SXES and NEXAFS analyses.

Name	H (at.%)	Ar (at.%)	Density (g/cm^3)	sp^3 (%)			
	ERDA/RBS		XRR	SXES	Classify	NEXAFS	Classify
N1–1	2	0.5	2.81	33.8 ± 0.6	a-C	24.0	a-C
N1–2	2	0.3	2.71	30.2 ± 4.3		30.3	
N1–3	3	0.2	2.69	33.4 ± 1.7		34.6	
T1–1	26	4	1.91	45.5 ± 0.3	a-C:H	30.4	a-C:H
T1–2	25	6	1.90	45.1 ± 1.7		22.6	
T1–3	24	4	1.83	46.0 ± 1.5		18.9	
T1–4	24	4	1.70	42.6 ± 5.1		27.5	
T2–1	24	5	1.43	44.6 ± 1.1	a-C:H	29.0	a-C:H
T2–2	23	4	1.66	40.7 ± 1.4		31.2	
T3–1	48	4	1.91	50.9 ± 2.3	ta-C:H/a-C:H	18.9	a-C:H
T3–2	51	3	1.86	50.8 ± 3.1	ta-C:H/a-C:H	18.3	a-C:H
T3–3	31	4	1.67	46.4 ± 1.4	a-C:H	18.9	a-C:H
T3–4	41	4	1.30	44.6 ± 1.0	a-C:H	22.0	a-C:H
T3–5	42	1	1.40	50.3 ± 2.3	ta-C:H/a-C:H	22.9	a-C:H
T3–6	43	4	1.92	48.8 ± 0.3	a-C:H	17.6	a-C:H
T3–7	47	4	1.74	48.7 ± 0.8	a-C:H	17.6	a-C:H
C1	20	–	2.01	20.9 ± 2.4	a-C:H	5.5	a-C:H
K1	5	–	2.81	64.4 ± 0.7	ta-C	59.5	ta-C
K2	20	–	2.37	59.5 ± 1.1	ta-C:H	40.9	a-C:H
K3	12	–	1.77	60.9 ± 0.3	ta-C:H	48.0	a-C:H
K4	30	–	2.03	76.5 ± 1.7	ta-C:H	20.7	a-C:H
K5	23	–	2.23	66.3 ± 0.8	ta-C:H	49.3	a-C:H
K6	20	–	2.09	55.7 ± 3.6	ta-C:H	45.9	a-C:H
K7	30	–	1.70	67.6 ± 3.8	ta-C:H	50.6	ta-C:H
K8	21	–	2.03	62.2 ± 7.0	ta-C:H	39.7	a-C:H
K9	30	–	1.85	72.1 ± 0.5	ta-C:H	59.0	ta-C:H
K10	20	–	2.04	64.5 ± 2.0	ta-C:H	42.8	a-C:H
W1	–	–	2.89	66.6 ± 1.0	ta-C	75.9	ta-C

samples at the UVSOR Synchrotron Facility (BL3U), Institute for Molecular Science, to obtain the C *K*-edge spectra.

SXES was employed to examine the fine structure of the valence band density of states in DLC films. The measurements were performed using a commercial SXES-extended range detector (JEOL, SS-94040SXES-ER) equipped with a variable line-spacing (VLS) grating (JEOL, JS300N), attached to a field-emission electron probe microanalyzer (FE-EPMA, JEOL, JXA-iHP200F). The take-off angle was set to 40°. Primary electron beam irradiation was conducted with an electron acceleration voltage of 5 kV and a probe current of 50 nA. Each measurement area was irradiated for 50 s, accumulating data over 10 cycles. Measurements were performed on 3 areas per sample to ensure statistical reliability, and the results were averaged to calculate standard deviation. The characteristic X-rays measured by SXES are emitted in the 95 to 800 eV range [51].

Both characterization techniques were performed on flat samples, ensuring a non-destructive analysis method.

2.4. Quantitative sp^3/sp^2 ratio by NEXAFS and SXES spectra

This section outlines the methodology used to extract the sp^3/sp^2 ratio from the NEXAFS and SXES spectra.

The NEXAFS analysis determined the sp^3/sp^2 ratio by quantitatively interpreting C *K*-edge spectra. Absolute photon energy calibration was achieved by aligning the isolated π* (C=C) peak of HOPG with the reference value of 285.4 eV, as reported in the literature [34]. The experimental spectra were fitted using a nonlinear least-squares fitting method, with an error step function applied at the C 1*s* ionization energy of 290 eV to represent the spectral features accurately. A Pre-edge resonance corresponding to the C 1*s* → π* (C=C) transition was observed at 285.4 eV, with potential contributions from π* (C≡C) if present. The high-energy edge transitions included σ* (C−H), σ* (C−C), σ* (C=C), and σ* (C≡C) at 287.6, 289.6, 293.7, and 300.2 eV, respectively. Contamination effects due to the local electronic structure, such as C and H in amorphous carbon films and oxygen from the environment, contributed to features observed at 286.3 eV (π*, C−OH), 288.5 eV (π*, C=O or C≡C), and 297.5 eV (σ*, C−O) [30–34].

The sp^3/sp^2 ratio was calculated by integrating the intensity of the π* (C=C) peak relative to the broad σ* peak, using the following Eq. (1):

$$sp^3 \Big/ sp^2 ratio = \left[1 - \left(\frac{I_{\pi^*,sample}}{I_{\Delta E,sample}} \cdot \frac{I_{\Delta E,ref}}{I_{\pi^*,ref}}\right)\right] \times 100 \quad (1)$$

Here, $I_{\pi^*,\,sample}$, and $I_{\pi^*,\,ref}$ are the areas of the π* (C=C) peak at 285.4 eV for the films and the HOPG reference, respectively. $I_{\Delta E,\,sample}$, and $I_{\Delta E,\,ref}$ denote the areas under the broad σ* peak within the 287–330 eV range [29]. A detailed comparison of the C *K*-edge NEXAFS spectra between HOPG and amorphous carbon films has been previously reported [48].

The SXES analysis determined the sp^3/sp^2 ratio by examining the normalized C *K*-emission spectra of DLC films in the energy range of 250–300 eV, with intensities scaled between 0 and 100. Gaussian peak fitting was employed to decompose the spectra and identify contributions from sp^3- and sp^2-configured carbon atoms. The sp^3-σ bonds were assigned to an energy level of 279 eV, while the sp^2-σ and sp^2-π bonds were observed at 277 eV and 282 eV, respectively. Carbon-hydrogen bonds, including −CH and =CH, were detected at 275 eV. The −CH bonds associated with sp^3-configured carbon appeared at higher emission energy (>275 eV) due to longer bond lengths of 0.110 nm. In contrast, the = CH bonds of sp^2-configured carbon were detected at lower emission energies (<275 eV) due to shorter bond lengths of 0.109 nm. Additional spectral features included two split peaks from the *s*-state of carbon orbital, along with contamination signals attributed to oxygen and nitrogen at energies of 270, 274, 264, and 265 eV, respectively [28,35–38].

The sp^3/sp^2 ratio was calculated using the following standardless Eq. (2):

$$sp^3 \Big/ sp^2 ratio = \frac{I_{sp^3}}{I_{sp^2}} \times 100 \quad (2)$$

I^3_{sp} and I^2_{sp} represent the integrated areas corresponding to the sp^3 and sp^2 fractions. Our organization's NEXAFS and NMR achieved and validated this method, which is used as a reference [48].

It is important to note that surface contamination, particularly from aliphatic hydrocarbons, can significantly influence the NEXAFS-derived sp^3/sp^2 ratio. This effect arises due to the surface sensitivity of NEXAFS, which probes a shallow information depth, making it susceptible to artifacts introduced by adsorbed contaminations. F. Mangolini et al. demonstrated that such aliphatic contamination leads to an overestimation of the σ* features, thus skewing sp^3 quantification in carbon-based materials [42,52]. In contrast, SXES, which has a greater information depth, is much less sensitive to these surface adsorbates. This supports the argument that SXES may provide a more representative measure of the bulk film bonding environment, especially in hydrogenated DLC films. Nonetheless, while surface contamination may affect absolute sp^3 quantification in NEXAFS, it is expected to have a relatively uniform impact across similar H-doped DLC samples. It thus does not fully explain the observed divergence in sp^3 content with varying H concentrations.

3. Results and discussion

3.1. Film characterizations

Fig. 1 presents the RBS and ERDA spectra of amorphous carbon films synthesized in the N1, T1, T2, T3, and C1 series. The RBS spectra display the relative yield (counts) and backscattered signals (channels) corresponding to carbon (C), argon (Ar), and silicon (Si) atoms, as identified through interactions with scattered He^+ particles. C signals appear in the 250–500 channel range, Ar signals in the 1100–1300 channel range, and Si signals from 850 to 1000 channels. In contrast, the ERDA spectra show the relative yield (counts) and recoiled signals for H atoms, observed within the 350–750 channel range.

Elemental quantitative analysis, particularly the determination of H content, was performed using the SIMNRA simulation applied to the ERDA spectra and cross-referenced with the RBS data. Films in the N1 Series (N1–1, N1–2, and N1–3) and K1 series consistently exhibited low H content (≤5 at.%), while Ar content varied among the N1 series, measured at 0.5, 0.3, and 0.2 at.%, respectively. The W1 film, deposited using a filtered cathodic vacuum arc (FCVA) system, was assumed to be hydrogen-free, as reported by Jing Wei [53].

For the T1 series, comprising films T1–1, T1–2, T1–3, and T1–4, a medium H content was detected, with values of 26, 25, 24, and 24 at.%, respectively. Ar content in these films measured 4, 6, 4, and 4 at.%, respectively. Similarly, the T2 series (T2–1 and T2–2) demonstrated medium H content, with values of 24 and 23 at.% and Ar content of 5 and 4 at.%, respectively. The T3 series films exhibited high H content, which varied significantly among the samples. H levels were measured as 48, 51, 31, 41, 42, 43, and 47 at.% for films T3–1, T3–2, T3–3, T3–4, T3–5, T3–6, and T3–7, respectively. Ar content within these films ranged from 1 to 4 at.%, with specific values of 4, 3, 4, 4, 1, 4, and 4 at.%, respectively.

Film in the K2-K10 series demonstrated medium to high H content, measured at 20, 12, 30, 23, 20, 30, 21, 30, and 20 at.%, respectively.

For the C1 series, the films exhibited a moderate H content of 20 at.%. Notably, no detectable Ar signal was observed in this sample. Fig. 2 shows a comparative plot of H and Ar content across all film series.

The varying H content across the N1, T1, T2, T3, C1, K1–10, and W1 series reflects the influence of deposition techniques and process parameters on the film composition. N1, K1, and W1 series exhibit low H content, approximately ≤5 at.%, characteristic of hydrogen-free PVD techniques and Ar-assisted deposition, leading to dense films [1,53,54].

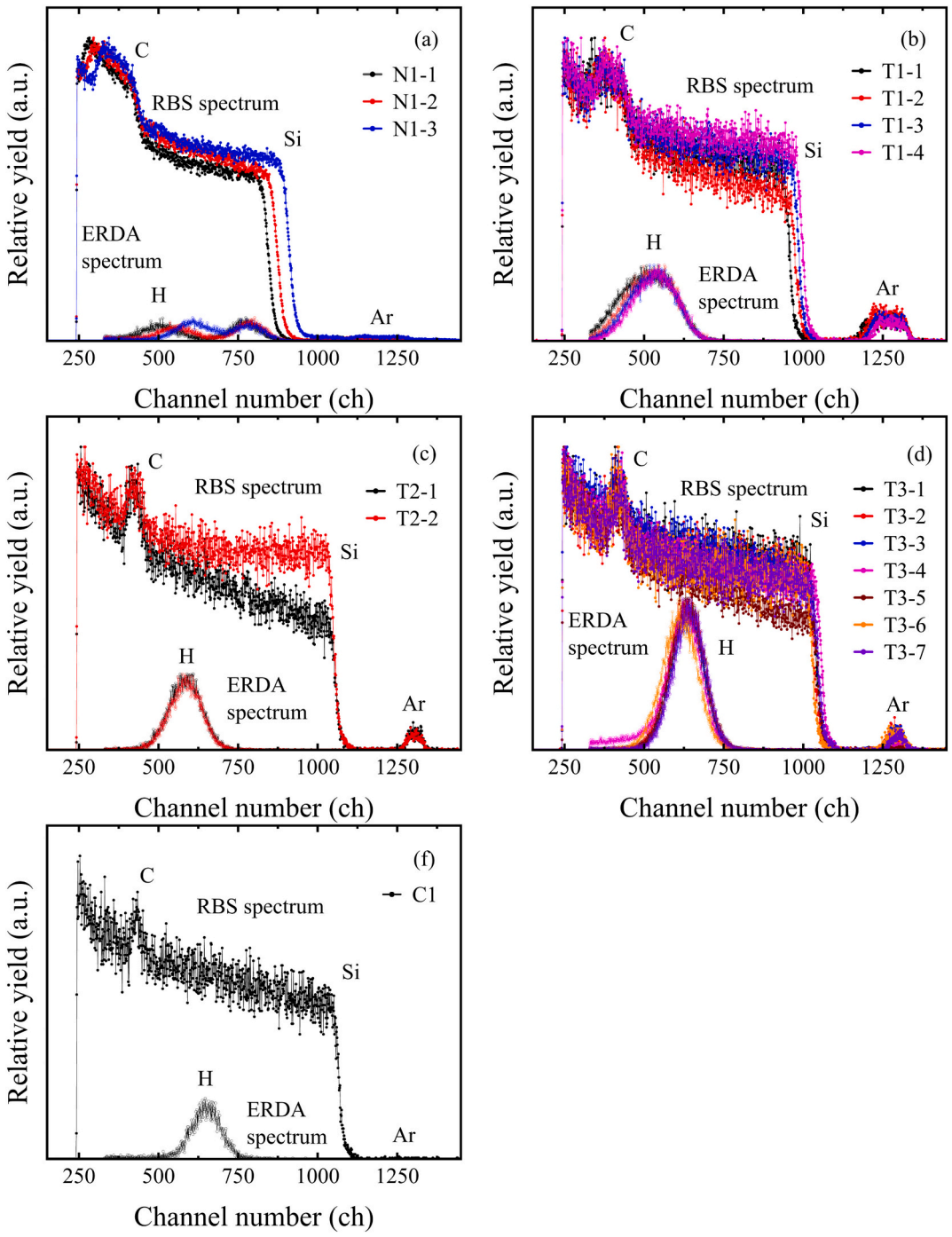

Fig. 1. RBS and ERDA spectra of DLC films for the N1, T1-T3 Series, and C1. Carbon signals are observed within the channel range 250–500, argon signals between 1100 and 1300, and silicon signals from 850 to 1000 channels. In contrast, the ERDA spectra show the relative yield (counts) and recoiled signals for hydrogen atoms, which appear within the channel range of 350–750.

T1, T2, T3, and K2–9 series films show medium to high H content (23 to 51 at.%), likely resulting from a controlled balance of hydrocarbon precursors and Ar by CVD techniques. T3, K4, K7, and K9 series films with the highest H content can have sp^3 content of up to 70 %. However, most sp^3 bonding is C−H bonds terminated, producing soft and low density. Nevertheless, the T1, T2, K2, K3, K5, K6, K8, and K10 series films with intermediate H content may have a lower overall sp^3 ratio, and these films contain more C−C bonds than the T3 series films. Thus, these films have better mechanical properties [1,11,20].

The case of a C1 series film is characterized by a moderate H content of 20 at.%. This finding suggests that the C1 film likely originated from multiple sources, as mentioned in the sample preparation, including residual hydrogen-containing gases in the sputtering chamber, surface adsorption on the target or Si wafer, trace impurities within the graphite target itself, or plasma interactions during deposition. Post-deposition exposure to air or moisture may also contribute [55,56]. Further analysis would be required to pinpoint these contributing factors.

The presence of Ar content in the N1, T1, T2, and T3 series reflects its role as a residual process gas from the deposition process. Ar atoms and ions play a crucial role in the deposition process, facilitating the dissociation of precursor molecules within the plasma sheath to generate activated species essential for the growth of DLC films. Without the

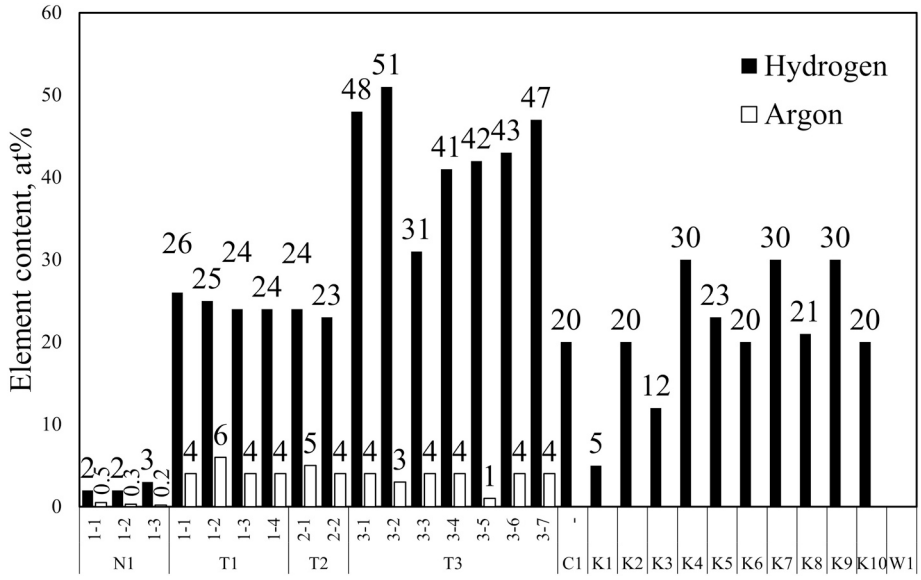

Fig. 2. Comparison of hydrogen content among the series. The N1 Series exhibits a hydrogen content of 2 to 5 at.%, while the T1-T3 series shows 24–26, 23–24, and 31–51 at.% hydrogen content, respectively. The C1 series exhibits a hydrogen content of 20 at.%. Films in the K2-K10 series demonstrated hydrogen content ranging from low to high, measured at 5–30 at.%.

introduction of Ar, the probability of precursor recombination increases, resulting in a reduced growth rate [57,58]. Furthermore, Ar ion bombardment contributes to film densification and enhances sp^3 bonding within the film structure [1,58]. The absence of detectable Ar in the C1 series highlights the distinct nature of the sputtering process, where Ar primarily functions to sputter carbon from a graphite electrode rather than being directly incorporated into the film. Previous studies, such as those by Z. Marinkovic and R. Roy, have reported that residual Ar levels of up to 6 at.% can increase film density, aligning with the trends observed in this study [22].

Fig. 3 illustrates the grazing incidence XRR profiles for the amorphous carbon film, highlighting the critical angles associated with the film densities (red arrows) and the Si substrate (black arrows). Most films, including the T1, T2, T3, and C1 series, exhibit densities lower than the Si substrates (2.33 g/cm^3 [59]), resulting in a double critical angle. The first critical angle, marked by the red arrow, corresponds to the film density. As the incidence angle exceeds this critical angle, X-rays penetrate the film, leading to a sudden decrease in reflectivity due to absorption, followed by reflection at the film-substrate interface. The interference between X-rays reflected at the surface and the interface generates oscillations known as Kiessig fringes [60]. In contrast, the N1 and W1 series, with densities exceeding that of the substrate, exhibit a single [59].

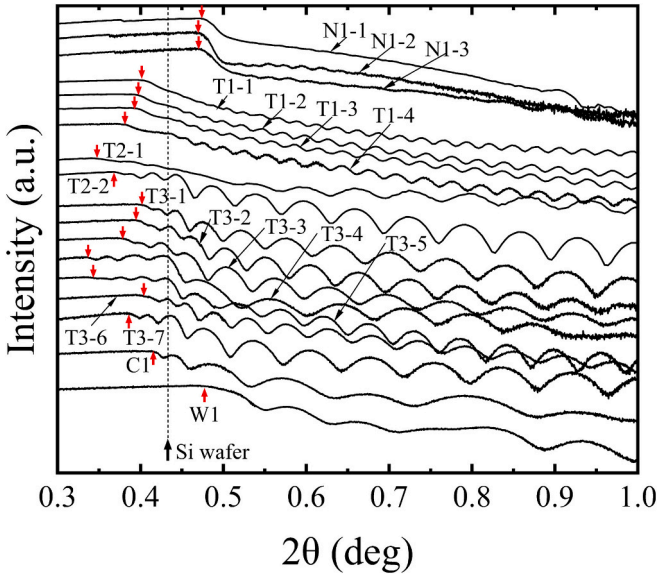

Fig. 3. XRR profiles for the DLC film, highlighting critical angles correlated with the film densities (red arrows) and the silicon substrate (black arrows). Most films in the T1, T2, T3, and C1 series exhibit densities lower than that of silicon substrates (2.33 g/cm^3 [59]), resulting in a double critical angle. In contrast, the N1 and W1 series, with densities exceeding that of the substrates, exhibit only a single critical angle.

Using a layer model in GlobalFit software, the experimental and simulated data achieved R-values between 0.02 and 0.10. The calculated densities are summarized in Fig. 4. The N1 Series (N1–1, N1–2, and N1–3), representing hydrogen-free DLC, exhibited the highest film density at 2.81 g/cm^3, 2.71 g/cm^3, and 2.69 g/cm^3, respectively. The W1 series, deposited via FCVA, also showed a relatively high film density at 2.89 g/cm^3. The T1 series (T1–1 to T1–4) displayed densities of 1.91 g/cm^3, 1.90 g/cm^3, 1.83 g/cm^3, and 1.70 g/cm^3, respectively, while the T2 series (T2–1, T2–2) showed densities of 1.43 g/cm^3 and 1.66 g/cm^3. The T3 series exhibited significant variation, with densities ranging from 1.30 to 1.92 g/cm^3 (T3–1 to T3–7). Finally, the C1 series films demonstrated a film density of 2.01 g/cm^3. These results reflect the structural variation across the hydrogenated DLC film.

The K series, K1, exhibits a 2.81 g/cm^3 density for the hydrogen-free DLC sample. In contrast, the hydrogenated K2 to K10 films display lower densities, ranging from 1.70 to 2.37 g/cm^3.

Film density is a crucial indicator of the H content within the DLC coatings, reflecting the microstructural characteristics influenced by deposition conditions. The N1, K1, and W1 series exhibit the highest densities (2.69 to 2.89 g/cm^3) and the lowest H content (≤5 at.%). These characteristics suggest a deposition process favoring a low dangling bond and a high sp^3 ratio [29] or a high sp^2 ratio with a smaller sp^2 cluster size [54]. In contrast, the T-series displays intermediate to high H content and lower densities. The T1 and T2 series (1.43 to 1.91 g/cm^3) trend demonstrates a balanced H incorporation (~25 at.%), likely achieved through a CVD process. The trend of higher density in the T1 and T2 series could be attributed to applying a higher bias voltage, favoring an increased sp^3 ratio with fewer voids [5].

The T3 series, characterized by the highest H content (31 to 51 at.%)

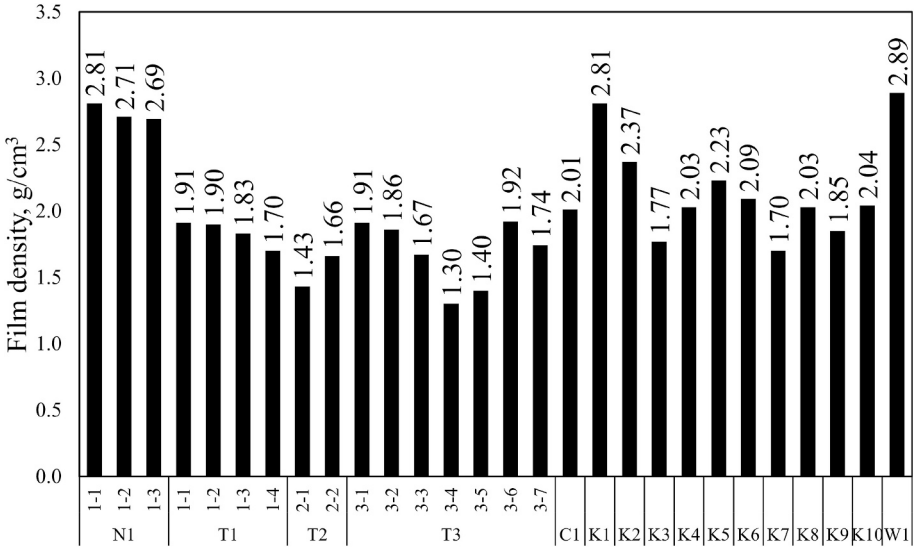

Fig. 4. Comparison of film densities for the N1, T1-T3, C1, K1–10, and W1 series. The densities range from 2.71 to 2.81 g/cm^3 for the N1 series, 1.70 to 1.91 g/cm^3 for the T1 series, 1.43 to 1.66 g/cm^3 for the T2 series, 1.30 to 1.92 g/cm^3 for the T3 series, 2.01 g/cm^3 for the C1 series, 1.70 to 2.81 g/cm^3 for the K1–10 series, and 2.89 g/cm^3 for the W1 series.

and correspondingly lower densities (1.30 to 1.92 g/cm^3), reflects a structure dominated by the sp^3 ratio with significant H termination. This H incorporation results in softer films due to a higher prevalence of dangling bonds and reduced atomic packing density [20]. The structural impact of H is further evident in the K2 to K10 films, which, although part of the same series as the dense, hydrogen-free K1 sample, display significantly lower densities (1.70 to 2.37 g/cm^3) consistent with hydrogenated DLC. H termination disrupts the carbon network, increases free volume, and reduces overall film compactness, consistent with the findings of Neuville and Matthews (2007) [26]. These trends align with those observed in the T series and K2-K10 series, reinforcing the relationship between H content and reduced film density. These findings support the ERDA results and confirm structural variation across the film series.

The C1 series, with a density of 2.01 g/cm^3, differs notably from the other series. This density and the sputtering deposition method suggest insufficient ion energy and flux reaching the growing film. Without applying a bias voltage in this method, it likely results in a lower sp^3 ratio and a more open microstructure [11]. These observations are consistent with existing literature, highlighting the significant role of ion energy, precursor gas composition, and H incorporation in determining the structural properties of amorphous carbon films. Films with low H content and high density are usually linked to deposition techniques promoting the sp^3 ratio. In contrast, hydrogen-rich films with lower densities indicate processes favoring the sp^2 ratio or the inclusion of voids [1,8].

3.2. Characteristics of electronic configurations by SXES and NEXAFS techniques

An arrangement of the SXES and NEXAFS spectra provides insights into the density of states (DOS) from the valence bands to the conduction bands. Fig. 5 combines the C *K*-emission SXES spectrum (bottom panel) and the C *K*-edge NEXAFS spectrum (top panel) for each sample, highlighting features associated with sp^2 and sp^3 bonding. These variations reflect differences in bonding configurations and deposition methods through differences in spectral shape.

The C *K*-emission spectra (photon energy range: 250 to 300 eV) exhibit a broad, prominent peak around 279 eV, a high-energy shoulder near 282 eV, and distinct features at photon energies below 277 eV. These spectra components suggest similar structural and chemical bonding characteristics across the amorphous carbon films, distinguishing them from graphite and diamond. A comparison of these spectra has been previously reported [48]. Variations in peak intensities and positions reflect differences in the relative ratios of bonding types (sp^2 and sp^3). This likely arises from variations in deposition techniques and parameters, as noted in earlier studies [36]. The SXES spectra within the series show minimal variation in intensity, indicating a consistent valence band structure across the films.

In contrast, the C *K*-edge spectra (photon energy range: 280 to 330 eV) show a consistent overall shape, characterized by two main features: a pre-edge resonance peak around 285.4 eV, attributed to transitions from the C 1*s* orbital to unoccupied π* orbitals and broad σ* resonances bands spanning 287 to 330 eV, arising from multielectron excitations. The pre-edge peak signified the presence of sp^2 bonding, while the σ* bands relate to the overall film structure, reflecting the contributions of sp^3 bonding and the surrounding carbon matrix [30]. Unlike the SXES spectra, NEXAFS spectra reveal more significant variation in the pre-edge resonance peak and σ* resonance intensity within the series, reflecting subtle differences in the film's electronic and structural properties.

The sp^3 content of the amorphous carbon films was determined using two techniques: NEXAFS and SXES. The NEXAFS method involves normalizing the C 1*s* transition resonance areas of π* at 285.4 eV to the broad σ* resonance bands spanning 287 to 330 eV. This method compares the results with a HOPG described in Eq. (1) (see Section 2.4). Conversely, the SXES approach calculates the sp^3 content by extracting the area fractions corresponding to sp^3-, sp^2-, −CH, and =CH bonds, as per Eq. (2). Fig. 6 presents an example of the deconvoluted spectrum for hydrogen-free and hydrogenated DLC films, displaying multiple peaks associated with NEXAFS and SXES analyses. The calculated sp^3 values for all samples are summarized in Fig. 7. The results show that NEXAFS and SXES yield comparable sp^3 values for hydrogen-free films (e.g., N1, K1, W1), supporting the reliability of both techniques in low-hydrogen environments. However, for hydrogenated films (T1-T3, K2-K10, C1), SXES consistently reports higher sp^3 content than NEXAFS. This discrepancy highlights the differential sensitivity of the techniques: SXES probes deeper and better captures bulk bonding states, whereas NEXAFS is more surface-sensitive and susceptible to hydrogen-induced distortions in the electronic structure. The comparative trends across the series reinforce the importance of using both methods for the characterization of sp^3/sp^2 hybridization, particularly in hydrogenated

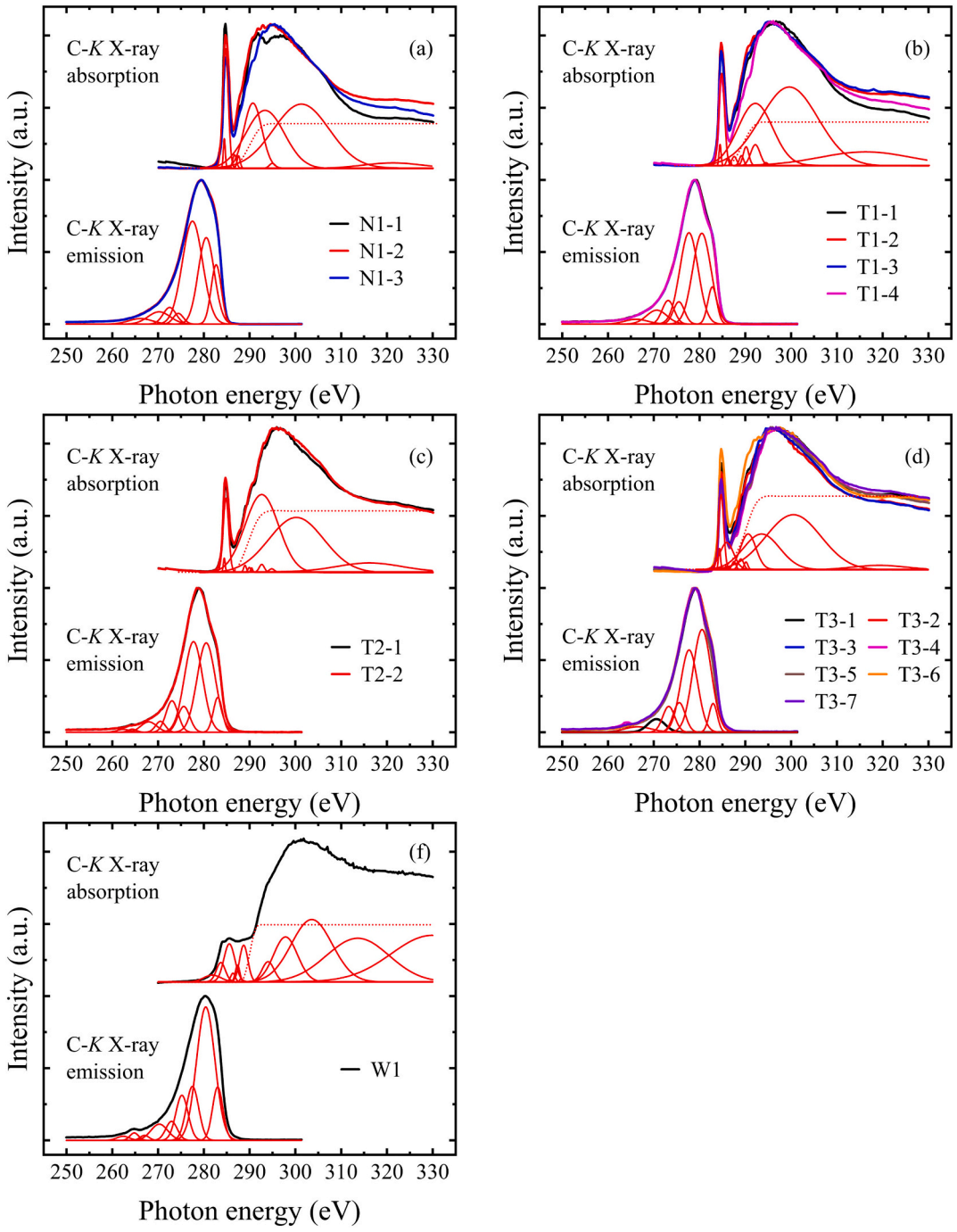

Fig. 5. The C 1*s* NEXAFS spectra of DLC films show an intensity proportional to the unoccupied state (top panel), while the C *K* SXES spectra probe the occupied electronic states (bottom panel) on N1, T1-T3, C1, and W1 series in (a)–(f).

amorphous carbon systems.

Fig. 8 compares the C *K* SXES spectra and C *K* NEXAFS spectra. Fig. 8 (a) illustrates the energy distribution in the valence band of hydrogen-free DLC films as the SXES spectra. This includes spectra for a high-sp^2 content film (black, N1 series) and a high-sp^3 content film (red, W1). A chemical shift is observed between the two: the high-sp^2 film shows a peak corresponding to the sp^2-σ site at approximately 277 eV, while the high sp^3 film shows a shift to higher energy, with a peak at the sp^3-σ site near 279 eV. Another noteworthy observation is the full width at half-maximum (FWHM) of the N1 series. Although the N1 series contains a high sp^2 content, the area under the sp^2-π at ~282 eV is not larger than that of the W1 series. This finding supports the earlier discussion in the density section, suggesting that the N1 series is composed of small sp^2 clusters despite its overall high sp^2 content. The use of FWHM as an indicator of molecular size is supported by the work of E. Tegeler [37]. Furthermore, the pre-edge resonance in the NEXAFS spectra, Fig. 8(b) at 285.4 eV, differentiates between high sp^2 content (N1 series) and high sp^3 content (W1 series). The N1 series exhibits a more intense pre-edge peak, consistent with findings reported by K. Kanda et al. [30–32].

Fig. 8(c) presents a comparison between hydrogen-free DLC and hydrogenated DLC films, each selected for having the highest sp^3 content as determined by the SXES technique. This comparison illustrates the influence of hydrogenation incorporation on the electronic structure. In hydrogenated DLC, H atoms terminate dangling bonds on sp^3-hybridized

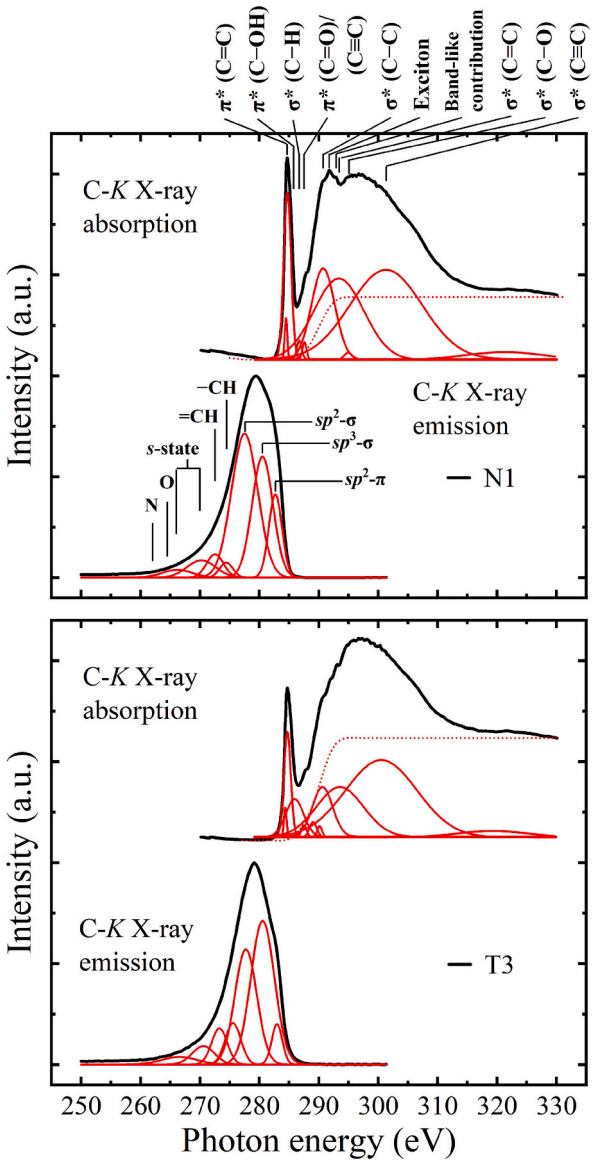

Fig. 6. NEXAFS C *K*-edge and SXES C *K*-emission spectra generated for (a) hydrogen-free and (b) hydrogenated DLC films. For NEXAFS, the error function step was applied to fit the edge jump at the ionization potential, as shown by the dotted red line. The SXES, the normalized C *K*-emission spectra at 250 to 300 eV, with intensities scaled between 0 and 100. Both spectra were deconvoluted into multiple Gaussian peaks.

carbon atoms, which stabilizes the tetrahedral (diamond-like) bonding structure, controls graphitization, and maintains a high sp^3 content, as reported by Grill (1999) and J. Robertson (2002) [1,24]. In sp^2-rich regions, H tends to terminate π-bonded carbon atoms at the edges of graphitic clusters, effectively reducing the cluster size and increasing film disorder (Neuville and Matthews, 2007) [26]. Accordingly, the SXES spectra for the hydrogenated DLC film show a spectral shift toward the sp^3-σ site near 279 eV, along with a reduced intensity in the sp^2-π shoulder in the ~282 eV range. A modest enhancement is also observed in the 275–276 eV range, which corresponds to C−H bond emissions. However, despite the significant difference in H concentrations observed by ERDA, the variation in this C−H region is limited. This suggests that while SXES has deeper probing capabilities and is less affected by surface contamination, it may still lack sufficient spectral resolution to capture the full variation in −CH and =CH bond content across different hydrogenation levels.

In contrast, Fig. 8(d) presents the NEXAFS spectra for the same samples. While NEXAFS provides valuable insights into near-surface electronic transitions, it shows reduced sensitivity to hydrogen incorporation, particularly in the region around 287.6 eV associated with σ* (C−H) transitions. Inconsistently, hydrogen-free films sometimes exhibit higher apparent absorption in this region, suggesting that overlapping features or interference from environmental oxygen species are present. These findings indicate that although SXES may offer a more representative picture of the bulk bonding environment, neither SXES nor NEXAFS alone fully resolves the C−H bonding signature in hydrogenated amorphous carbon films. Therefore, complementary techniques such as FT-IR or nuclear reaction analysis (NRA) are recommended to elucidate further the role of H in altering the bonding configuration.

Fig. 8(e) compares hydrogenated DLC films with medium and high H content, further emphasizing the structural role of H as discussed previously. In SXES spectra, films with higher H content exhibit a noticeable reduction in the sp^2-π shoulder intensity around ~282 eV, reflecting a decrease in the size or prevalence of sp^2-bonded clusters. Simultaneously, the emission intensity in the 275–276 eV range, associated with C−H bonds, is significantly enhanced, indicating a higher degree of H incorporation. Conversely, the NEXAFS spectra, Fig. 8(f), demonstrate limited sensitivity to increasing H content. As H concentration rises, the spectra fail to proportionally reflect this change, underscoring NEXAFS's reduced capacity to detect C−H bonding contributions in hydrogen-rich DLC films.

Comparing the sp^3 content measured by NEXAFS and SXES reveals notable trends across the film series, analyzed using beamlines at Synchrotron Light Research Institute (BL3.2U), Thailand, and the UVSOR Synchrotron Facility (BL3U), Japan. Fig. 9(a) and (b) illustrate that in hydrogen-free films (N1, K1, W1), sp^3 values from both techniques are in close agreement, consistent with ERDA measurements showing insignificant hydrogen content. However, discrepancies emerge in hydrogenated films (T1-T3, K2–10, and C1 series), where NEXAFS consistently underestimates sp^3 content relative to SXES.

One contributing factor may be the surface sensitivity of NEXAFS, which is more susceptible to hydrocarbon contamination and surface-adsorbed aliphatic species, known to distort π* and σ* resonance features and reduce the apparent sp^3 signal, especially in the presence of ambient air exposure [42]. In contrast, SXES is a bulk-sensitive technique with a greater information depth, which minimizes the influence of surface contamination and better captures the overall bonding configuration throughout the film volume.

The term "broader regions" here refers to the larger sampling volume probed by SXES, encompassing both near-surface and deeper subsurface regions. The expression "more effectively" implies that SXES, under its depth profiling and emission-based analysis of occupied states, captures a more representative average of sp^3 bonding in the bulk film, especially where local disorder or H-induced defects vary with depth. Prior studies [16,47,61–63] have demonstrated SXES's strength in identifying bonding hybridization across heterogeneous amorphous carbon films.

While ERDA solely quantifies H content, the trends observed in SXES correlate more instinctively with the increasing H fractions: higher H incorporation tends to stabilize sp^3 bonding by terminating dangling bonds, aligning with the rising sp^3 fractions measured by SXES. Conversely, NEXAFS trends indicate a decrease in sp^3 with increasing H, which may reflect a reduction in the effects or limitations of resolving C−H environments near the surface. Therefore, although ERDA does not directly measure sp^3, its H quantification supports the reliability of the SXES-derived sp^3 trend over that of NEXAFS in hydrogenated films.

As both NEXAFS and SXES are non-destructive and surface-sensitive techniques, no evidence of C−H bond breakage was observed during sample preparation for either analysis [52]. The discrepancy in sp^3 content between NEXAFS and SXES can be attributed to several factors, including H sensitivity, sample homogeneity, surface contamination, and differences in probing depth. As shown in Fig. 9, this discrepancy becomes more pronounced at higher H concentrations, suggesting that H

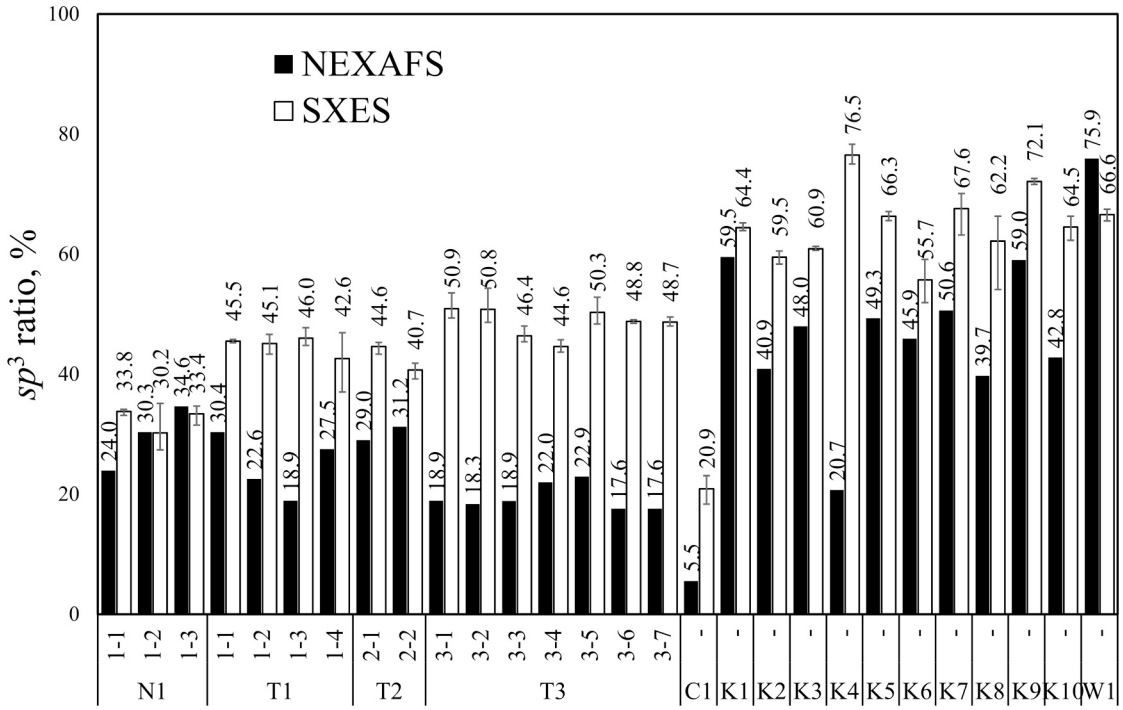

Fig. 7. The sp^3 ratio was calculated using SXES and NEXAFS. From NEXAFS analysis and SXES, the sp^3 contents are as follows: N1, T1-T3, C1, K1-K10, and W1 series.

incorporation affects the measurement sensitivity of each technique. NEXAFS relies on near-surface excitation of core-level (C 1*s*) electrons into unoccupied π* and σ* orbitals [39,52,64], This surface-sensitive nature makes it more susceptible to H-induced electronic distortion and surface-adsorbed hydrocarbons, often resulting in underestimation of sp^3 content in H-rich films [16,47,61]. In contrast, SXES probes photon emissions originating from deeper within the material, corresponding to transitions from occupied C 2*p*-states to the C 1*s* core hole [9,51,65]. This is further supported by the higher detection of C−H bond fractions in SXES spectra compared to NEXAFS, as shown in Table 2. The enhanced depth sensitivity and spectral integration of SXES reduce its susceptibility to surface H enrichment and dangling bonds, thereby explaining its consistently higher sp^3 content estimates [38,48,51,65]. While both techniques reveal consistent qualitative trends regarding the effects of H content and deposition technique, their discrepancies highlight the necessity for further investigation. Future work should address how deposition parameters influence near-surface versus bulk properties in amorphous carbon films, and how these effects impact advanced spectroscopic analysis and our understanding of hydrogen's structural role.

Table 3 further supports this distinction; the relative C−H emission intensities from SXES exhibit good correlation with H/C atomic ratios measured independently by ERDA, especially for the N, T1, and T2 film series. This suggests SXES can serve as a semi-quantitative tool for assessing hydrogenation trends in DLC films. Discrepancies observed at high H (T3 series) likely reflect SXES limitations, such as spectral overlap at low H concentrations or signal delocalization and damping effects under high H saturation [66].

While SXES cannot substitute for ERDA in precise H quantification, it offers valuable insight into relative H incorporation and bonding states, especially when interpreted in conjunction with NEXAFS data. These results are consistent with the higher C−H bonding intensity observed in SXES compared to NEXAFS (see Table 2), reinforcing the conclusion that SXES provides a stronger characterization of the overall bonding network in hydrogenated films.

These distinctions highlight the necessity of employing complementary spectroscopic techniques to evaluate amorphous carbon materials accurately and underscore the need for further investigation into how deposition parameters shape both surface and bulk bonding environments [38,48,51,65].

Importantly, SXES and NEXAFS are governed by different selection rules and probe fundamentally different electronic states, occupied (valence band) vs. unoccupied (conduction band), respectively. The relative contribution of *s*- and *p*-like states to these bands may differ, especially in amorphous systems. Therefore, expecting a one-to-one correspondence in sp^3/sp^2 ratios between the 2 techniques assumes equal density of *p*-states in both occupied and unoccupied bands, which is not physically guaranteed. As such, the discrepancies shown in Fig. 7 should not be attributed solely to H incorporation. These intrinsic methodological differences highlight the importance of using both techniques in a complementary manner. An uncertainty margin of ±5–20 % in the estimated sp^3 content is reasonable, considering factors such as spectral deconvolution variability, differences in electronic structure sensitivity, and residual surface contamination [9,42,48].

3.3. Impact on amorphous carbon film applications

The study's conclusion emphasizes the significance of the H content and sp^3/sp^2 ratio, defining the bonding characteristics of DLC films, which, according to prior studies, are closely linked to mechanical properties and practical applications. The NEXAFS and SXES techniques enable the precise characterization of the sp^3 ratio, reflecting microstructural differences in films produced under various deposition methods and conditions. Particularly in mechanically demanding categories such as ta-C (50–90 % sp^3, H ≤ 5 %) and ta-C:H (50–90 % sp^3, 5–50 % H), these films are excellent for tribological systems, biomedical devices, and protective coatings. Increased hardness, wear resistance, and chemical inertness are all associated with higher sp^3 content. Conversely, films with a higher sp^2 content, such as a-C (20–50 % sp^3, H ≤ 5 %) and a-C:H (20–50 % sp^3, 5–50 % H), are typically classified as mechanically soft and exhibit enhanced electrical conductivity and flexibility, which are advantageous for flexible displays and electronic components [2,4,11].

Discrepancies between the results from NEXAFS and SXES further

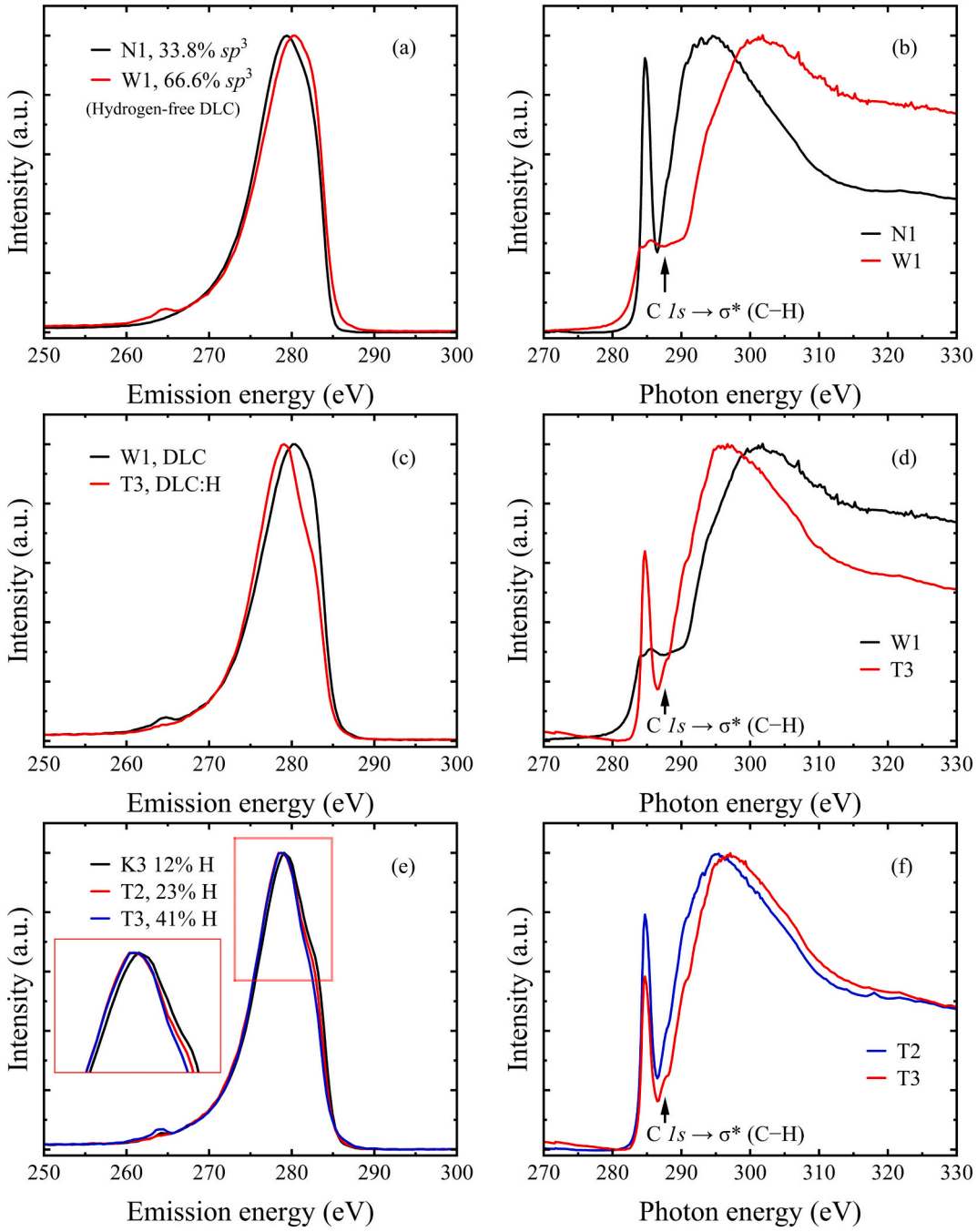

Fig. 8. Comparison of SXES and NEXAFS spectra for various DLC films: (a) and (b) present hydrogen-free DLC films with low and high sp^3 content; (c) and (d) compare hydrogen-free and hydrogenated DLC films with the highest sp^3 content; (e) and (f) show DLC films with medium and high hydrogen content.

underscore the importance of employing complementary characterization techniques to optimize deposition processes and ensure accurate classification based on application-specific requirements, as demonstrated in Table 1 using sp^3 ratio and H content. Specifically, in hydrogenated DLC films, inconsistencies often arise due to inherent limitations of the NEXAFS technique. This technique tends to underestimate the sp^3 fraction in hydrogenated films, as it is less sensitive to C−H bonds. Consequently, hydrogenated DLC films may be misclassified as a-C:H, despite SXES data indicating a higher sp^3 character. In contrast, SXES, which probes the electronic structure more comprehensively and is less influenced by H or surface effects, often provides a more accurate assessment of bonding configurations. Therefore, for reliable classification of hydrogenated DLC films, especially those with high H content, SXES should be used in conjunction with NEXAFS to ensure strong and representative characterization.

Additionally, film density and the sp^3/sp^2 ratio are valuable indicators of the characteristics, mechanical performance, and potential applications of both hydrogen-free and hydrogenated DLC films. The density of diamond is approximately 50 % higher than that of graphite, primarily due to the layered structure of graphite, which results in a lower packing efficiency. This distinction carries over into the amorphous phase of carbon, as seen in DLC, which contains a mixed sp^3/sp^2 network [1,4]. Accordingly, a linear correlation exists between density and the sp^3/sp^2 ratio. As the sp^3 content increases, particularly in ta-C films, the Young's modulus and hardness approach values typical of crystalline diamond [1]. However, the presence of H complicates this

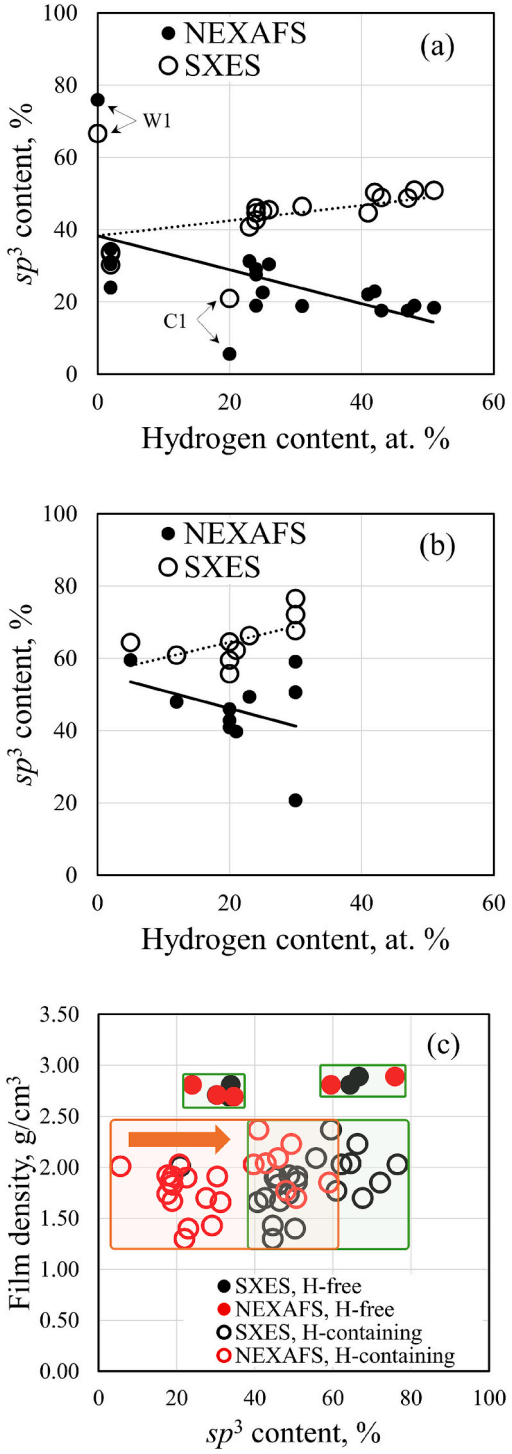

Fig. 9. Comparison of sp^3 content measured by NEXAFS and SXES across all film series. (a) NEXAFS measurements conducted at the Synchrotron Light Research Institute (BL3.2U), Thailand, and (b) at the UVSOR Synchrotron Facility (BL3U), Institute for Molecular Science, Japan. (c) Comparison of sp^3 content obtained via NEXAFS and SXES as a function of film density.

relationship. The C−H bond occupies a significant volume, reducing the film's density and hardness. For example, ta-C:H films, which are sp^3-rich and contain approximately 20 at.% H typically exhibit lower density compared to ta-C, which often shows densities around 2.4 g/cm^3 [1,59]. While the density of ta-C:H still scales with sp^3 content, it does so at a lower baseline due to the inclusion of H. In contrast, sp^2-rich hydrogenated films (a-C:H) typically exhibit lower densities, ranging from approximately 2.0 g/cm^3. These films can be broadly categorized into two groups based on their density: those with a density above 2.0 g/cm^3 and those with a density below 2.0 g/cm^3. Films with around 20 at.% H tend to have densities above 2.0 g/cm^3, while those with more than 40 at.% H falls below this threshold [11].

The comparison of results obtained via NEXAFS and SXES, as shown in Fig. 9(c), further highlights the importance of employing complementary techniques. While both methods are effective in estimating the sp^3 content, their respective limitations become especially apparent in hydrogenated samples. NEXAFS often underestimates sp^3 content due to limited sensitivity to C−H bonding and surface sensitivity, potentially leading to misclassification. SXES, on the other hand, samples deeper regions and is less influenced by surface contaminations and aliphatic terminations, yields a more reliable estimation of the overall sp^3 fraction.

Interestingly, the density versus sp^3 content plot in Fig. 9(c) does not display the strong positive correlation typically reported in amorphous carbon films, such as that shown in Fig. 11 of Ferrari et al. [59]. This discrepancy likely arises from several contributing factors. First, hydrogen incorporation affects film density independently of sp^3 hybridization by introducing microvoids and terminating dangling bonds, which reduces mass density while stabilizing the network [1,24,26]. Second, the films in this study were synthesized via diverse techniques (PVD, CVD, FCVA, and sputtering), resulting in microstructural heterogeneity and variable hydrogen content, both of which decouple the conventional density-sp^3 trend [17,67]. Third, differences in measurement depth and sensitivity between NEXAFS and SXES, especially in hydrogenated films with surface-bound species or inhomogeneous bonding, further contribute to the observed scatter [46,68,69]. Nonetheless, Fig. 9(c) effectively distinguishes between hydrogen-free and hydrogen-containing films, indicating that hydrogen content plays a central role in both density and bonding configurations. This observation highlights the need for depth-sensitive, multi-technique characterization to elucidate the structure-property relationship in DLC films.

In summary, the accurate classification and design of DLC films, particularly those that are hydrogenated, rely on the complementary use of SXES and NEXAFS. Future work should focus on refining deposition strategies and further elucidating the complex interactions between H incorporation, bonding configurations, and film properties. These efforts will enhance the utility of amorphous carbon films in high-performance applications that require precise mechanical and electronic properties.

4. Conclusion

This study highlights the interpretation of sp^3/sp^2 bonding, H content, and deposition techniques in amorphous carbon films. NEXAFS and SXES offer complementary insights. Due to network termination effects, NEXAFS, being more sensitive to unoccupied π* and σ* orbitals near the surface, may underestimate the sp^3 fraction in hydrogenated films. In contrast, SXES reflects the overall bonding environment, capturing a broader integration of sp^3-, sp^2-, and hydrogenated states. Our study emphasizes the role of H in shifting the local electronic structure and sp^3/sp^2 ratios, significantly impacting film properties. Low H content films showed consistent results between the methods, while hydrogen-rich films revealed discrepancies linked to H's influence on the local electronic structure. These findings underscore the importance of precise characterization and deposition control in designing amorphous carbon films for advanced applications. Further research should refine these techniques to better understand H's role in film properties.

CRediT authorship contribution statement

Thitikorn Chamchuang: Investigation, Formal analysis, Data curation, Writing – review & editing, Writing – original draft. **Tsuneo Suzuki:** Methodology, Formal analysis. **Sarayut Tunmee:** Investigation, Formal analysis, Writing – review & editing. **Praphaphon**

Table 2
Through curve fitting of the NEXAFS and SXES spectra, CH bonds (NEXAFS, C 1*s* → σ* of C−H at 287.6 eV and SXES carbon-hydrogen bonds, including −CH and =CH at around 275 eV), CC bonds, and other bonding types were compared.

Samples	NEXAFS (%)			SXES (%)			
	CH bonds	CC bonds	Contaminations (O, N, etc.)	CH bonds	CC bonds	*s* state	Contaminations (O, N, etc.)
N1	0.5	98.8	0.7	6.8	84.8	8.4	–
N2	0.0	98.0	2.0	4.9	88.2	6.9	–
N3	0.6	98.7	0.8	7.0	85.0	8.0	–
T11	0.5	98.6	0.9	11.7	79.6	8.7	–
T12	0.2	97.4	2.4	13.3	78.6	8.1	–
T13	0.4	98.9	0.7	12.9	79.1	8.0	–
T14	1.5	95.9	2.6	12.9	79.1	8.0	–
T21	0.3	99.3	0.5	14.9	77.9	5.9	1.4
T22	1.7	98.1	0.3	11.5	80.1	8.5	–
T31	6.1	72.1	21.8	14.7	77.1	8.2	–
T32	0.7	98.2	1.1	13.7	78.5	7.8	–
T33	0.2	88.6	11.2	14.1	78.7	6.3	0.9
T34	0.2	90.9	8.8	13.8	78.5	5.6	2.1
T35	0.1	98.8	1.0	18.4	75.9	4.3	1.3
T36	2.3	97.1	0.6	13.8	78.0	8.2	–
T37	3.1	91.9	5.0	14.2	76.9	8.9	–
C1	0.8	98.4	0.8	15.1	76.9	5.9	2.1
W1	0.6	98.9	0.4	15.8	75.3	6.6	2.4

Table 3
Provides a comparison between ERDA-derived H/C atomic ratios and SXES-derived relative C−H intensities.

Samples	H/C atomic ratio (ERDA/RBS) (Average)	H/C atomic ratio (SXES) (Average)
N series	0.02	0.09
T1 series	0.25	0.23
T2 series	0.24	0.24
T3 series	0.43	0.27

Remark: SXES derived by H/C ratio calculated from H/C = [3(−CH) + 1/2 (=CH)] / [(3(−CH) + 1/2(=CH) + (—C) + (=C)].

Silawong: Investigation, Formal analysis, Writing – review & editing. **Peng Guo:** Investigation, Formal analysis. **Kazuhiro Kanda:** Investigation, Formal analysis, Data curation, Writing – review & editing. **Keiji Komatsu:** Investigation, Formal analysis, Writing – review & editing. **Hidetoshi Saitoh:** Supervision, Methodology, Conceptualization, Writing – review & editing. **Aiying Wang:** Writing – review & editing.

Declaration of competing interest

The authors declare that they have no known competing financial interests or personal relationships that could have appeared to influence the work reported in this paper.

Acknowledgments

The authors gratefully acknowledge the Extreme Energy-Density Research Institute and the Optoelectronic Ceramics Laboratory at Nagaoka University of Technology, Japan, for providing access to advanced instrumentation, including the 1.7 MV Tandetron accelerator (HVEE, model 4117MC+). Appreciation is also extended to the BL3.2Ub beamline of the Synchrotron Light Research Institute (SLRI), a public organization in Nakhon Ratchasima, Thailand, and to the UVSOR Synchrotron Facility BL3U at the Institute for Molecular Science, for their valuable support of this research. Their expertise and unwavering assistance were instrumental in facilitating the experiments and analyses conducted in this study. The authors further acknowledge Prof. Aiying Wang and Prof. Kazuhiro Kanda for kindly providing the data and samples W1 and K1-10 used in this study. Additionally, Aiying Wang and Peng Guo would like to acknowledge the financial support from the National Natural Science Foundation of China (No. U24A2030).

Data availability

No data was used for the research described in the article.

References

[1] J. Robertson, Diamond-like amorphous carbon, Mater. Sci. Eng. R. Rep. 37 (4) (2002) 129–281, https://doi.org/10.1016/S0927-796X(02)00005-0.
[2] N. Ohtake, et al., Properties and classification of diamond-like carbon films, Materials 14 (2021) 315, https://doi.org/10.3390/ma14020315.
[3] J. Robertson, Amorphous carbon, Adv. Phys. 35 (4) (1986) 317–374, https://doi.org/10.1080/00018738600101911.
[4] J. Robertson, Properties of diamond-like carbon, Surf. Coat. Technol. 50 (3) (1992) 185–203, https://doi.org/10.1016/0257-8972(92)90001-Q.
[5] N. Konkhunthot, et al., The correlation between optical and mechanical properties of amorphous diamond-like carbon films prepared by pulsed filtered cathodic vacuum arc deposition, Thin Solid Films 653 (2018) 317–325, https://doi.org/10.1016/j.tsf.2018.03.053.
[6] H. Tashiro, M. Nakaya, A. Hotta, Enhancement of the gas barrier property of polymers by DLC coating with organosilane interlayer, Diam. Relat. Mater. 35 (2013) 7–13, https://doi.org/10.1016/j.diamond.2013.03.001.
[7] A. Ilie, et al., Photoconductivity and electronic transport in tetrahedral amorphous carbon and hydrogenated tetrahedral amorphous carbon, J. Appl. Phys. 84 (10) (1998) 5575–5582, https://doi.org/10.1063/1.368602.
[8] J. Robertson, The deposition mechanism of diamond-like a-C and a-C: H, Diam. Relat. Mater. 3 (4) (1994) 361–368, https://doi.org/10.1016/0925-9635(94)90186-4.
[9] T. Chamchuang, et al., Effect of 200 MPa-compressive hydrogens on the microstructure of diamond-like carbon coatings, Diam. Relat. Mater. (2025) 111971, https://doi.org/10.1016/j.diamond.2025.111971.
[10] J. Vetter, 60 years of DLC coatings: historical highlights and technical review of cathodic arc processes to synthesize various DLC types, and their evolution for industrial applications, Surf. Coat. Technol. 257 (2014) 213–240, https://doi.org/10.1016/j.surfcoat.2014.08.017.
[11] H. Saitoh, Classification of diamond-like carbon films, Jpn. J. Appl. Phys. 51 (9R) (2012) 090120, https://doi.org/10.1143/JJAP.51.090120.
[12] W. Jacob, W. Möller, On the structure of thin hydrocarbon films, Appl. Phys. Lett. 63 (13) (1993) 1771–1773, https://doi.org/10.1063/1.110683.
[13] L. Zhang, et al., A ternary phase diagram for amorphous carbon, Carbon 94 (2015) 202–213, https://doi.org/10.1016/j.carbon.2015.06.055.
[14] B. Schultrich, Hydrogenated amorphous carbon films (a-C:H), in: B. Schultrich (Ed.), Tetrahedrally Bonded Amorphous Carbon Films I: Basics, Structure and Preparation, Springer Berlin Heidelberg, Berlin, Heidelberg, 2018, pp. 111–192.
[15] N. Dwivedi, et al., Correlation of sp3 and sp2 fraction of carbon with electrical, optical and nano-mechanical properties of argon-diluted diamond-like carbon films, Appl. Surf. Sci. 257 (15) (2011) 6804–6810, https://doi.org/10.1016/j.apsusc.2011.02.134.
[16] E. Staryga, G.W. Bąk, Relation between physical structure and electrical properties of diamond-like carbon thin films, Diam. Relat. Mater. 14 (1) (2005) 23–34, https://doi.org/10.1016/j.diamond.2004.06.030.
[17] K. Bewilogua, D. Hofmann, History of diamond-like carbon films — from first experiments to worldwide applications, Surf. Coat. Technol. 242 (2014) 214–225, https://doi.org/10.1016/j.surfcoat.2014.01.031.

[18] A. Erdemir, C. Donnet, Tribology of diamond-like carbon films: recent progress and future prospects, J. Phys. D. Appl. Phys. 39 (18) (2006) R311, https://doi.org/10.1088/0022-3727/39/18/R01.
[19] M. Tamura, T. Kumagai, Hydrogen permeability of diamondlike amorphous carbons, J. Vac. Sci. Technol. A 35 (4) (2017) 04D101, https://doi.org/10.1116/1.4977106.
[20] C. Casiraghi, A.C. Ferrari, J. Robertson, Raman spectroscopy of hydrogenated amorphous carbons, Phys. Rev. B 72 (8) (2005) 085401, https://doi.org/10.1103/PhysRevB.72.085401.
[21] A. Shirakura, et al., Diamond-like carbon films for PET bottles and medical applications, Thin Solid Films 494 (1) (2006) 84–91, https://doi.org/10.1016/j.tsf.2005.08.366.
[22] Z. Marinkovic, R. Roy, Preparation and properties of sputtered “glassy” carbon films, Carbon 14 (6) (1976) 329–331, https://doi.org/10.1016/0008-6223(76)90005-1.
[23] R. Hauert, A review of modified DLC coatings for biological applications, Diam. Relat. Mater. 12 (3) (2003) 583–589, https://doi.org/10.1016/S0925-9635(03)00081-5.
[24] A. Grill, Diamond-like carbon: state of the art, Diam. Relat. Mater. 8 (2) (1999) 428–434, https://doi.org/10.1016/S0925-9635(98)00262-3.
[25] F.Z. Cui, D.J. Li, A review of investigations on biocompatibility of diamond-like carbon and carbon nitride films, Surf. Coat. Technol. 131 (1) (2000) 481–487, https://doi.org/10.1016/S0257-8972(00)00809-4.
[26] S. Neuville, A. Matthews, A perspective on the optimisation of hard carbon and related coatings for engineering applications, Thin Solid Films 515 (17) (2007) 6619–6653, https://doi.org/10.1016/j.tsf.2007.02.011.
[27] P. Zimmermann, et al., Modern X-ray spectroscopy: XAS and XES in the laboratory, Coord. Chem. Rev. 423 (2020) 213466, https://doi.org/10.1016/j.ccr.2020.213466.
[28] E.Z. Kurmaev, et al., X-ray emission spectra of carbon materials, Carbon 24 (3) (1986) 249–253, https://doi.org/10.1016/0008-6223(86)90224-1.
[29] N. Konkhunthot, P. Photongkam, P. Wongpanya, Improvement of thermal stability, adhesion strength and corrosion performance of diamond-like carbon films with titanium doping, Appl. Surf. Sci. 469 (2019) 471–486, https://doi.org/10.1016/j.apsusc.2018.11.028.
[30] K. Kanda, et al., NEXAFS study on substrate temperature dependence of DLC films formed by Ar cluster ion beam assisted deposition, Nucl. Instr. Meth. Phys. Res. B 206 (2003) 880–883, https://doi.org/10.1016/S0168-583X(03)00888-7.
[31] K. Kanda, et al., Characterization of hard diamond-like carbon films formed by Ar gas gluster ion beam-assisted fullerene deposition, Jpn. J. Appl. Phys. 41 (6S) (2002) 4295, https://doi.org/10.1143/JJAP.41.4295.
[32] T. Kitagawa, et al., Near edge X-ray absorption fine structure study for optimization of hard diamond-like carbon film formation with Ar cluster ion beam, Jpn. J. Appl. Phys. 42 (6S) (2003) 3971, https://doi.org/10.1143/JJAP.42.3971.
[33] A. Saikubo, et al., Comprehensive classification of DLC films formed by various methods using NEXAFS measurement, Diam. Relat. Mater. 17 (7) (2008) 1743–1745, https://doi.org/10.1016/j.diamond.2008.01.095.
[34] P.E. Batson, Carbon 1s near-edge-absorption fine structure in graphite, Phys. Rev. B 48 (4) (1993) 2608–2610, https://doi.org/10.1103/PhysRevB.48.2608.
[35] Y. Ma, et al., Soft-x-ray resonant inelastic scattering at the C K edge of diamond, Phys. Rev. Lett. 69 (17) (1992) 2598–2601, https://doi.org/10.1103/PhysRevLett.69.2598.
[36] G. Wiech, et al., Diamond-like hydrogenated amorphous carbon films studied by X-ray emission spectroscopy, Diam. Relat. Mater. 6 (8) (1997) 944–951, https://doi.org/10.1016/S0925-9635(97)00005-8.
[37] E. Tegeler, G. Wiech, A. Faessler, Carbon K-emission spectra and electronic structure of solid naphthalene and anthracene, J. Phys. B At. Mol. Phys. 14 (8) (1981) 1273, https://doi.org/10.1088/0022-3700/14/8/012.
[38] M. Aono, et al., Photoinduced deformation of a-C thin films prepared by RF magnetron sputtering, Diam. Relat. Mater. 108 (2020) 107844, https://doi.org/10.1016/j.diamond.2020.107844.
[39] C. Lenardi, et al., Near-edge x-ray absorption fine structure and raman characterization of amorphous and nanostructured carbon films, J. Appl. Phys. 85 (10) (1999) 7159–7167, https://doi.org/10.1063/1.370527.
[40] A.T. Kozakov, et al., Determination of sp2 and sp3 phase fractions on the surface of diamond films from C1s, valence band X-ray photoelectron spectra and CKVV X-ray-excited Auger spectra, Appl. Surf. Sci. 536 (2021) 147807, https://doi.org/10.1016/j.apsusc.2020.147807.
[41] H. Gyulasaryan, et al., Graphene clusters in carbon: structural features and magnetic properties, Appl. Surf. Sci. 687 (2025) 162284, https://doi.org/10.1016/j.apsusc.2024.162284.
[42] F. Mangolini, et al., Accounting for nanometer-thick adventitious carbon contamination in X-ray absorption spectra of carbon-based materials, Anal. Chem. 86 (24) (2014) 12258–12265, https://doi.org/10.1021/ac503409c.
[43] J.H. Kim, et al., Tailored hydrogen-free carbon films by tuning the sp2/sp3 configuration, ACS Appl. Electron. Mater. 3 (4) (2021) 1771–1779, https://doi.org/10.1021/acsaelm.1c00046.
[44] J. Robertson, Gap states in diamond-like amorphous carbon, Philos. Mag. B 76 (3) (1997) 335–350, https://doi.org/10.1080/01418639708241098.
[45] D. Das, Chapter Five - Nanocrystalline Diamond: A High-Impact Carbon Nanomaterial for Multifunctional Applications Including as Nanofiller in Biopolymeric Matrice, in: S. Yaragalla, et al. (Eds.), Carbon-Based Nanofillers and Their Rubber Nanocomposites, Elsevier, 2019, pp. 123–181.
[46] J.H. Comfort, L.M. Garverick, R. Reif, Silicon surface cleaning by low dose argon-ion bombardment for low-temperature (750 °C) epitaxial silicon deposition. I. Process considerations, J. Appl. Phys. 62 (8) (1987) 3388–3397, https://doi.org/10.1063/1.339301.
[47] X. Zhou, et al., Quantitative NEXAFS and solid-state NMR studies of sp3/(sp2+sp3) ratio in the hydrogenated DLC films, Diam. Relat. Mater. 73 (2017) 232–240, https://doi.org/10.1016/j.diamond.2016.09.026.
[48] T. Chamchuang, et al., Novel method for quantifying the ratios of sp/sp hybridized carbon in diamond-like carbon films using soft X-ray emission spectroscopy, Diam. Relat. Mater. 150 (2024) 111742, https://doi.org/10.1016/j.diamond.2024.111742.
[49] M. Mayer, SIMNRA, a simulation program for the analysis of NRA, RBS and ERDA, AIP Conf. Proc. 475 (1) (1999) 541–544, https://doi.org/10.1063/1.59188.
[50] M. Yasaka, X-ray thin-film measurement techniques V. X-ray reflectivity measurement, Rigaku J. 26 (2010) 1–9.
[51] H. Takahashi, et al., Development of soft X-ray emission spectrometer for EPMA/SEM and its application, IOP Conf. Ser. Mater. Sci. Eng. 109 (1) (2016) 012017, https://doi.org/10.1088/1757-899X/109/1/012017.
[52] F. Mangolini, et al., Quantification of the carbon bonding state in amorphous carbon materials: a comparison between EELS and NEXAFS measurements, Carbon 173 (2021) 557–564, https://doi.org/10.1016/j.carbon.2020.11.021.
[53] J. Wei, et al., Corrosion resistance of amorphous carbon film in 3.5 wt% NaCl solution for marine application, Electrochim. Acta 346 (2020) 136282, https://doi.org/10.1016/j.electacta.2020.136282.
[54] R. Miyamoto, et al., Optical constants of diamond-like carbon films formed by gas cluster ion beam assisted deposition, Appl. Phys. Express 15 (3) (2022) 035501, https://doi.org/10.35848/1882-0786/ac4e28.
[55] C.F. Adame, et al., Amorphous carbon thin films: mechanisms of hydrogen incorporation during magnetron sputtering and consequences for the secondary electron emission, J. Vac. Sci. Technol. A 41 (4) (2023) 043412, https://doi.org/10.1116/6.0002759.
[56] N. Bundaleski, et al., The role of hydrogen incorporation into amorphous carbon films in the change of the secondary electron yield, Int. J. Mol. Sci. 24 (16) (2023), https://doi.org/10.3390/ijms241612999.
[57] R.G. Toro, et al., Argon and hydrogen plasma influence on the protective properties of diamond-like carbon films as barrier coating, Surf. Interfaces 6 (2017) 60–71, https://doi.org/10.1016/j.surfin.2016.11.009.
[58] A. Costa, et al., Effect of hydrogen incorporation on the mechanical properties of DLC films deposited by HiPIMS in DOMS mode, Surf. Coat. Technol. 473 (2023) 129980, https://doi.org/10.1016/j.surfcoat.2023.129980.
[59] A.C. Ferrari, et al., Density, sp3 fraction, and cross-sectional structure of amorphous carbon films determined by x-ray reflectivity and electron energy-loss spectroscopy, Phys. Rev. B 62 (16) (2000) 11089–11103, https://doi.org/10.1103/PhysRevB.62.11089.
[60] H. Kiessig, Untersuchungen zur totalreflexion von röntgenstrahlen, Ann. Phys. 402 (6) (1931) 715–768, https://doi.org/10.1002/andp.19314020607.
[61] N. Fourches, G. Turban, Plasma deposition of hydrogenated amorphous carbon: growth rates, properties and structures, Thin Solid Films 240 (1–2) (1994) 28–38, https://doi.org/10.1016/0040-6090(94)90689-0.
[62] Y. Sato, et al., Electron energy-loss and soft X-ray emission spectroscopy of electronic structure of MgB4, J. Solid State Chem. 253 (2017) 58–62, https://doi.org/10.1016/j.jssc.2017.05.007.
[63] M. Aono, et al., Deposition of amorphous carbon nitride thin films using pressure-gradient RF magnetron sputtering and their chemical bonding structures, Appl. Surf. Sci. 635 (2023) 157677, https://doi.org/10.1016/j.apsusc.2023.157677.
[64] R. Hansson, et al., Opportunities and challenges in probing local composition of organic material blends for photovoltaics, J. Mater. Res. 32 (10) (2017) 1982–1992, https://doi.org/10.1557/jmr.2017.7.
[65] M. Terauchi, Development of TEM-SXES instruments for valence electron spectroscopy, Microsc. Microanal. 15 (S2) (2009) 214–215, https://doi.org/10.1017/S1431927609096081.
[66] R.F. Egerton, P. Li, M. Malac, Radiation damage in the TEM and SEM, Micron 35 (6) (2004) 399–409, https://doi.org/10.1016/j.micron.2004.02.003.
[67] A.G. Salek, et al., The structure and electronic properties of tetrahedrally bonded hydrogenated amorphous carbon, Appl. Phys. Lett. 122 (18) (2023) 181904, https://doi.org/10.1063/5.0147494.
[68] Y. Muramatsu, et al., Soft X-ray emission and absorption spectra in the C K region of sputtered amorphous carbon films, Carbon 39 (9) (2001) 1403–1407, https://doi.org/10.1016/S0008-6223(00)00260-8.
[69] X. Liu, W. Yang, Z. Liu, Recent progress on synchrotron-based in-situ soft X-ray spectroscopy for energy materials, Adv. Mater. 26 (46) (2014) 7710–7729, https://doi.org/10.1002/adma.201304676.